Amino Acids (2015) 47:357–367
DOI 10.1007/s00726-014-1868-y

ORIGINAL ARTICLE

Trafficking of excitatory amino acid transporter 2-laden vesicles in cultured astrocytes: a comparison between approximate and exact determination of trajectory angles

Chapin E. Cavender · Manoj K. Gottipati · Vladimir Parpura

Received: 10 October 2014 / Accepted: 3 November 2014 / Published online: 19 November 2014

Abstract A clear consensus concerning the mechanisms of intracellular secretory vesicle trafficking in astrocytes is lacking in the physiological literature. A good characterization of vesicle trafficking that may assist researchers in achieving that goal is the trajectory angle, defined as the angle between the trajectory of a vesicle and a line radial to the cell's nucleus. In this study, we provide a precise definition of the trajectory angle, describe and compare two methods for its calculation in terms of measureable trafficking parameters, and give recommendations for the appropriate use of each method. We investigated the trafficking of vesicles containing excitatory amino acid transporter 2 (EAAT2) fluorescently tagged with enhanced green fluorescent protein (EGFP) to quantify and validate the precision of each method. The motion of fluorescent puncta—taken to represent vesicles containing EAAT2-EGFP—was found to be typical of secretory vesicle trafficking. An exact method for calculating the trajectory angle of these puncta produced no error but required large computation time. An approximate method reduced the requisite computation time but produced an error depending on the inverse of the ratio of the punctum's initial distance from the nucleus centroid to its maximal displacement. Fitting this dependence to a power function allowed us to establish an exclusion distance from the centroid, beyond which the approximate method is less likely to produce an error above an acceptable 5 %. We recommend that the exact method be used to calculate the trajectory angle for puncta closer to the nucleus centroid than this exclusion distance.

Keywords Glutamate transporters · Trafficking · Angle · Diffusion coefficient · GFAP

Abbreviations

CB1R	Cannabinoid receptor 1
DIC	Differential interference contrast
EAAT2	Excitatory amino acid transporter 2
EGFP	Enhanced green fluorescent protein
Emd	Emerald green fluorescent protein
FITC	Fluorescein isothiocyanate
GFAP	Glial fibrillary acidic protein
HBSS	Hank's balanced salt solution
IQR	Interquartile range
pro-ANP	pro-Atrial natriuretic peptide
RT	Room temperature
TGN	Trans-Golgi network

Electronic supplementary material The online version of this article (doi:10.1007/s00726-014-1868-y) contains supplementary material, which is available to authorized users.

C. E. Cavender (✉) · M. K. Gottipati · V. Parpura (✉)
Department of Neurobiology, University of Alabama, Birmingham, 1719 6th Ave S, CIRC429, Birmingham, Alabama 35294, United States
e-mail: chapinc@uab.edu

V. Parpura
e-mail: vlad@uab.edu

C. E. Cavender
Department of Physics, University of Alabama, Birmingham, 1719 6th Ave S, CIRC429, Birmingham, Alabama 35294, United States

M. K. Gottipati · V. Parpura
Department of Biomedical Engineering, University of Alabama, Birmingham, 1719 6th Ave S, CIRC429, Birmingham, Alabama 35294, United States

V. Parpura
Department of Biotechnology, University of Rijeka, 51000 Rijeka, Croatia

Introduction

Research in the past two decades has shown that astrocytes, a type of glial cell and likely the most numerous cells in the mammalian brain, have central roles in the structural and functional development and in the maintenance of homeostasis of the nervous system (Nedergaard et al. 2003; Parpura and Verkhratsky 2012). One of their primary roles is the removal of excess neurotransmitter molecules from the extracellular space, particularly in the vicinity of synaptic sites. While neurotransmitters mediate typical signaling between neural cells and are critical for the normal functioning of the nervous system, excessive buildup of these molecules outside of the cells can have deleterious consequences. For example, the major excitatory amino acid neurotransmitter glutamate can cause neuronal death when present in high concentrations in the extracellular space (Lau and Tymianski 2010). This condition, known as excitotoxicity, has been implicated in the progression of neurodegenerative diseases such as Alzheimer's disease (Hynd et al. 2004) and Alexander disease (Tian et al. 2010).

Astrocytes provide a principal pathway for the uptake of glutamate. About 80 % of all glutamate released during synaptic transmission is taken up by astrocytes, while most of the remaining 20 % is taken up by post-synaptic neurons (Danbolt 2001; Hertz et al. 1999; Rothstein et al. 1996). This uptake of glutamate by mature astrocytes is accomplished by the plasma membrane sodium-dependent excitatory amino acid transporter (EAAT) 2 (Furuta et al. 1997), which are trafficked to the plasma membrane by secretory vesicles along the tracts in the cytoskeleton (Hughes et al. 2004). The uptake of glutamate from the extracellular space by astrocytes is dependent on the successful trafficking of these glutamate transporters to the plasma membrane, and disruptions in this trafficking may be responsible for some of the accumulation of glutamate in the extracellular space that has been associated with excitotoxic events. Hence, a better understanding of the trafficking characteristics of these secretory vesicles could provide an insight into their role in the regulation of glutamate uptake and the progression of neurodegenerative diseases.

A good characterization of secretory vesicle trafficking is the trajectory angle, defined as the angle between the trajectory of a vesicle and a vector in the radial direction away from the nucleus of the cell (Osborne et al. 2009). This parameter is useful for defining a preferred direction of motion for the vesicles whose motion cannot be described by simple diffusion. Indeed, it has been instrumental in discovering a preference for radial trafficking—i.e., motion directly toward or away from the nucleus—of vesicles carrying fluorescently tagged cannabinoid receptor 1 (CB1R) in rat astrocytes (Osborne et al. 2009). However, the trajectory angle has not been well studied in trafficking literature, and the means by which it is determined for individual vesicles have not been clearly articulated. Consequently, the goal of this paper is to describe a method for the determination of trajectory angles of secretory vesicles.

We studied the trafficking characteristics of vesicles containing fluorescently tagged EAAT2 in cultured mouse cortical astrocytes and used two methods for calculating the trajectory angles of these vesicles, which we describe in detail. We compared the results of these methods to those of previous trafficking studies to validate the methodology used. We also propose a few guidelines for the appropriate use of these methods in future analyses of trafficking of secretory vesicles.

Some of the data presented in this manuscript have appeared in preliminary form elsewhere (Cavender et al. 2013).

Materials and methods

Ethical approval

All procedures were in strict accordance with the National Institutes of Health Guide for Care and Use of Laboratory Animals and were approved by the University of Alabama, Birmingham Institutional Animal Care and Use Committee. The procedures also conform to the principles of UK regulations (Drummond 2009).

Purified astrocytic cell culture

Purified astrocytic cultures were made as described elsewhere (Gottipati et al. 2012; Reyes et al. 2011). Mice (C57BL/6 strain) were kept in ventilated cages at room temperature (RT, 20 °C–24 °C) under a 12-h light cycle (6 am On and 6 pm Off). Only one animal, a 0- to 2- day-old pup, at a time was removed from the colony and decapitated. Visual cortices from four pups of either sex were isolated and treated with papain (20 IU mL^{-1}; Sigma-Aldrich, St. Louis, MO, USA) in the presence of L-cysteine (0.2 mg mL^{-1}) for 1 h at 37 °C. Cortices were then treated with trypsin inhibitor (type II-O, 10 mg mL^{-1}; Sigma-Aldrich) for 5 min at RT to neutralize the enzymatic activity of papain and triturated in cell culture media using a glass serological pipette until no visible clumps appeared. The resulting cell suspension was plated into 25 cm^2 tissue culture flasks and left for 1 h at 37 °C in a 95 % air/5 % CO_2 atmosphere incubator to allow for cell attachment, after which the flasks were washed with Hank's balanced salt solution (HBSS, Life Technologies). The HBSS was replaced with cell culture media containing α-minimum essential medium (without phenol red; Gibco™, Life Technologies Corp., Grand Island, NY, USA) supplemented with fetal bovine serum (10 % v/v, HyClone™, Thermo

Fisher Scientific Inc., Waltham, MA, USA), sodium bicarbonate (14 mM), sodium pyruvate (1 mM), D-glucose (20 mM), L-glutamine (2 mM), penicillin (100 IU mL^{-1}), and streptomycin (100 μgmL^{-1}) (pH 7.35). The flasks were returned to the incubator and the cells were allowed to grow and proliferate for 10–14 days to reach approximately 60 % confluency, after which the flasks were purified for astrocytes using a previously described procedure (McCarthy and de Vellis 1980). The flasks were washed with ice cold cell culture media to kill the neurons and side-tapped to detach the microglia, dead neurons, and debris. The flasks were then shaken twice on a horizontal orbital shaker at 37 °C and 260 rpm, first for 1.5 h followed by two exchanges with ice cold cell culture media and then again for 18 h. This method yields purified astrocytes (>99 %), as we described elsewhere (Montana et al. 2004). At this juncture, purified astrocytes attached to the flask were detached using trypsin (10,000 N_{α}-benzoyl-L-arginine ethyl ester hydrochloride units mL^{-1}; Invitrogen™) diluted in HBSS for 2–3 min and pelleted by centrifugation for 10 min at 100×*g*. The pellet was resuspended in cell culture media, plated onto precleaned round glass coverslips (D-263 borosilicate glass, Erie Scientific Company; purchased via Fisher Scientific, catalog no. 12-545-82-12CIR-1D, 12 mm in diameter) coated with polyethyleneimine (1 mg mL^{-1}) (Lee and Parpura 2012), inlayed in plastic tissue culture dishes (round, 35 mm in diameter) containing 4 segments—each segment receiving one coverslip—and returned to the incubator for 1 h, after which the cell suspension was replaced with cell culture media. Dishes/cells were returned to the incubator until further use.

Transfection

The cells were transfected 1 day after plating with an EAAT2-EGFP plasmid (kindly provided by Dr. Jeffrey D. Rothstein, The Johns Hopkins University, Baltimore, MD, USA) encoding EAAT2 (containing a single amino acid mutation, G417D) tagged at its C-terminus with enhanced green fluorescent protein (EGFP). Each dish received 1 µg of the plasmid and 2 µL of TransIT-293 (Mirus Bio, LLC, Madison, WI, USA), premixed as per manufacturer's instructions. After 4 h, the dishes were washed with HBSS, which was replaced with fresh cell culture media. The dishes were returned to the incubator for 3 days until used in experiments.

Image acquisition

Coverslips containing cultured astrocytes were mounted onto an imaging chamber filled with an aqueous external solution (pH 7.4) consisting of sodium chloride (140 mM), potassium chloride (5 mM), calcium chloride (2 mM), magnesium chloride (2 mM), D-glucose (5 mM), and HEPES (10 mM) at RT and standard atmospheric pressure. An inverted microscope (Nikon TE300) equipped with differential interference contrast (DIC; halogen lamp, 100 W) and wide-field epifluorescence illumination (xenon arc lamp, 100 W) was used with a standard fluorescein isothiocyanate (FITC) filter set and a 60× Plan Apochromatic oil-immersion objective (numerical aperture, 1.4) to visualize the cells expressing EAAT2-EGFP. DIC imaging was used to visualize the cell boundaries and nuclei. The Rayleigh transverse and axial resolutions of the objective were calculated to be 233 and 833 nm, respectively, at the 535-nm emission wavelength. Still images and time-lapse images were acquired using a CoolSNAP®-HQ cooled charge coupled device camera (Photometrics, Tucson, AZ, USA) driven by MetaMorph® 6.1 imaging software (Molecular Devices, Chicago, IL, USA). One pixel corresponds to a square with 104.7 nm sides.

Analysis of vesicle trafficking

Analysis of the trafficking of intracellular vesicles (appearing as intracellular fluorescent puncta) was performed using MetaMorph® imaging software. Time-lapse images of individual cells taken at 1.2 frames s^{-1} for 40 s were filtered using a smoothing kernel—referred to as background flattening in MetaMorph®—to accentuate the edges, resulting in false-shading images. Subsequently, an intensity threshold—which was determined independently for each cell so that the maximum number of puncta was included without causing speckling in the cell background and apparent plasma membrane—was applied to these images. At this juncture, puncta, whose edge intensities exceeded the set threshold value and whose area was between 4 and 70 pixels, were selected for analysis, and the coordinates of their centroids were obtained in each frame. Of note, an apparent fluorescent punctum size exceeds that of the physical object studied, i.e., a trafficking vesicle reported to be approximately 300 nm in diameter in live astrocytes (Malarkey and Parpura 2011; Singh et al. 2014). For brevity, we shall refer to the coordinates of the centroid of a punctum as the position of the punctum. Puncta located fewer than 10 pixels (approximately 1 µm) from the lateral plasma membrane or from large aggregates (area greater than 70 pixels), puncta that could not be tracked in every frame, and puncta whose paths intersected those of other puncta were excluded from the analysis. Trafficking data for each punctum was analyzed using a custom Visual Basic script in Microsoft® Excel. The script calculated the maximal displacement (the greatest distance between any two points in the punctum's trajectory), mean instantaneous speed (the mean of the speeds of the punctum for each time step), track length (the sum of the distance traveled by the

punctum in each time step), and trajectory angle for each punctum and plotted the trajectory of the punctum with respect to the centroid of the nucleus. If a vesicle moves a distance Δr in a step time Δt, then the mean instantaneous speed is defined by $\langle \Delta r/\Delta t \rangle$, and the track length is defined by $\Sigma(\Delta r)_i$. ImageJ software version 1.47 (NIH, Washington, DC, USA) was used to hand trace the outline of the nuclear region based on the DIC image of the cell and to calculate the centroid of the nucleus as well as the maximum and minimum radii of the nucleus.

Error simulations

Simulations of the error associated with the difference between the two methods for calculating the trajectory angle were performed using MATLAB® software version R2013a (MathWorks, Natick, MA, USA). MATLAB® was also used to visually present the error found in experimental data in two-dimensional and three-dimensional plots.

Statistics

All reported quantities are expressed as a median with interquartile range (IQR) or a mean ± standard error. Normality of the distributions was assessed using the D'Agostino test. Unimodality was assessed using Hartigan's dip test (Hartigan and Hartigan 1985). Mann–Whitney *U* test was used to compare mean instantaneous speeds between the groups; the number of subjects required for comparison was estimated using power analysis (set at 80 % and $\alpha = 0.05$). All statistical analysis was performed using GB-STAT version 6.5 (Dynamic Microsystems, Inc., Silver Spring, MD, USA) except for tests of unimodality, which were performed using the dip test package in R version 3.0.2 (The R Foundation for Statistical Computing).

Results

Vesicle tracking

Visualization of cultured astrocytes expressing EAAT2-EGFP revealed that fluorescent puncta are distributed throughout the cell with greater apparent density in the cell periphery (Fig. 1a), which is thinner than 1 μm (Haydon et al. 1996) and is well suited for vesicular trafficking (Osborne et al. 2009; Potokar et al. 2005). Astrocytes displaying bright fluorescence were selected for analysis. Cell nuclei, visualized by DIC imaging (Fig. 1b), were elliptical in shape. The maximum and minimum nuclear radii and the coordinates of the nucleus centroid were calculated for each cell. For 15 cells analyzed, the median maximum nuclear radius was 7.0 μm (interquartile range 4.8–8.8 μm), and the median minimum nuclear radius was 2.9 μm (IQR 2.1–3.6 μm).

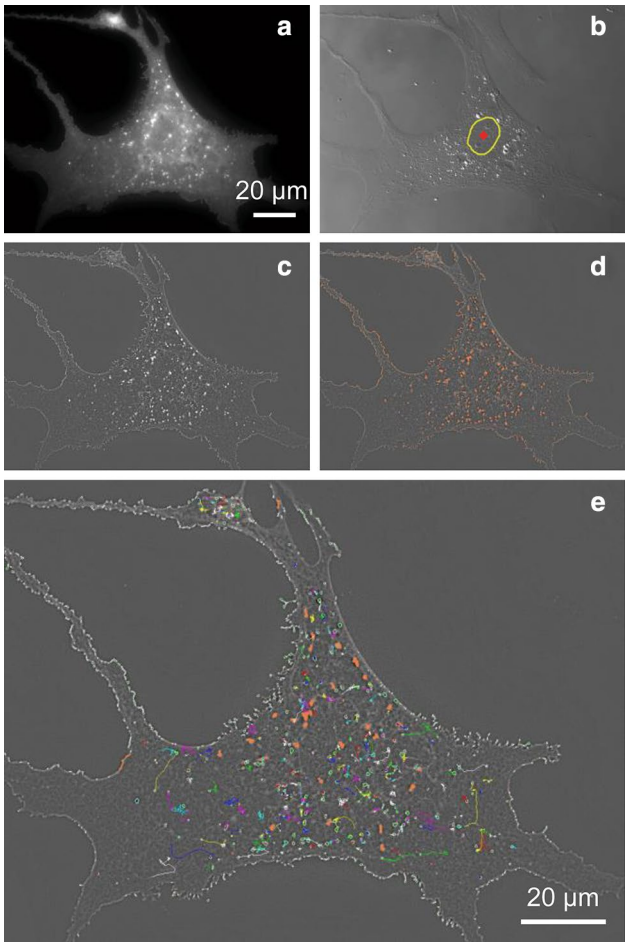

Fig. 1 Visualization and tracking of EAAT2-EGFP vesicles in cultured astrocytes. **a** A typical astrocyte expressing EAAT2-EGFP and imaged using a fluorescein isothiocyanate filter set to visualize the fluorescent puncta. **b** The cell shown in **a** imaged under differential interference contrast to disclose the nucleus. The *yellow curve* represents the trace of the nucleus, and the *red* rhombus represents the centroid of the nucleus. **c** Kernel-smoothened false-shading image of the fluorescence image shown in **a**. **d** An operative intensity threshold applied to the image shown in **c**. Puncta whose edge fluorescence intensities exceeded the threshold are identified in *orange*. **e** Composite motility of puncta from the 40 s time-lapse acquisition (Online Resource 1). *Colored curves* (other than *orange*) represent the trajectories of all the puncta superimposed onto the false-shading image shown in **d** (color figure online)

Tracking of intracellular vesicles/puncta was performed on time-lapse images, lasting 40 s, of individual astrocytes (Online Resource 1). Each image frame was kernel smoothened to obtain the corresponding false-shading image (Fig. 1c), to which an operative threshold was applied to define putative puncta (Fig. 1d, orange). The trajectories of the puncta that did not meet the exclusion criteria described in "Materials and methods", whose edge

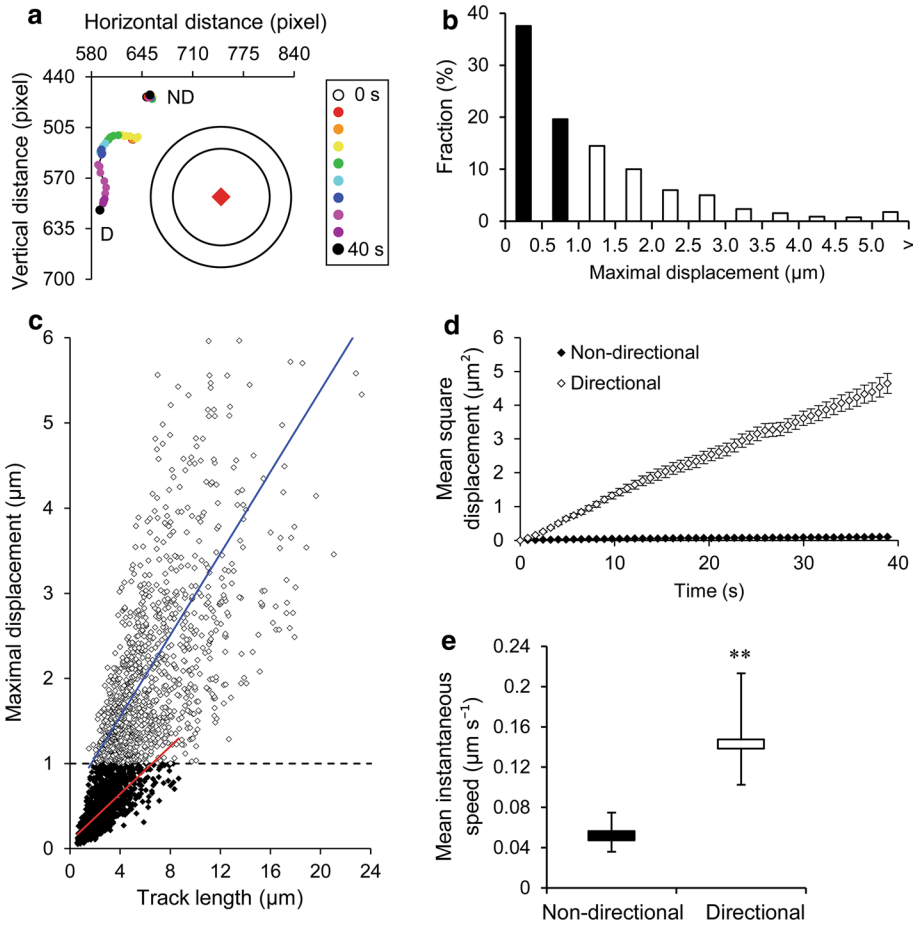

Fig. 2 Trafficking parameters for EAAT2-EGFP puncta. **a** Examples of typical trajectories of non-directional (ND, maximal displacement 0.81 μm) and directional (D, maximal displacement 11.1 μm) EAAT2-EGFP secretory vesicles. Trajectories are color coded by time (see *inset*). The *red* rhombus represents the nucleus centroid, and the *black concentric circles* show the maximum and minimum nuclear radius for the cell containing the sample trajectories. **b** Frequency distribution of maximal displacements as a percentage of all puncta (n = 2,593 for 15 cells); *black* and *open bars* represent non-directional and directional puncta, respectively. **c** Maximal displacement as a function of track length. The *solid lines* show the best-fit lines for non-directional vesicles (*red*, below *dashed line*, slope 0.139 ± 0.003, which represents the directionality index) and directional vesicles (*blue*, above *dashed line*, slope 0.240 ± 0.009). **d** Mean square displacement of the vesicles as a function of time. *Points* represent mean ± standard error. **e** Comparison of mean instantaneous speeds of non-directional (n = 1,483) and directional (n = 1,110) vesicles. *Boxes* represent median values ± interquartile range. *Asterisks* indicate a statistical difference between the groups (Mann–Whitney U test; $^{**}p < 0.0001$) (color figure online)

intensities exceeded the threshold value, and whose areas were between 4 and 70 pixels were obtained (Fig. 1e).

Characterization of EAAT2-EGFP vesicle trafficking

After image acquisition and tracking of vesicles, trafficking parameters—including maximal displacement, mean instantaneous speed, total track length, and trajectory angle—were determined for each punctum using original algorithms. Puncta were classified into two categories based on the magnitude of their maximal displacement. An average-sized secretory vesicle diffusionally moving through the cytoplasm can traverse at most a distance of 1 μm (Haydon et al. 1996) in the 40-s timeframe of our experiments (Osborne et al. 2009; Potokar et al. 2005). Thus, puncta whose maximal displacement was less than 1 μm were classified as non-directional, and their motion is assumed to be governed by simple diffusion; puncta whose maximal displacement was greater than 1 μm were classified as directional, and their motion is assumed to be governed by active transport along cytoskeletal elements (Potokar et al. 2005).

Examples of typical trajectories for these two categories of puncta are shown in Fig. 2a. The majority of puncta (57 %; 1,483 of 2,593 puncta) were classified as non-directional based on their maximal displacement (Fig. 2b). The directionality index, defined as the ratio of the maximal displacement of a puncta to its track length, was assessed by calculating the slope of the best-fit line for the plot of

maximal displacement of puncta against their track length using linear regression (Fig. 2c). The directionality index of directional puncta (0.240) was greater than that of non-directional puncta (0.139), suggesting that directional puncta exhibit a wider range of movement than non-directional puncta.

For a random walk model of simple diffusion, it can be shown from Fick's second law of diffusion (Einstein 1905) and from Monte Carlo simulations (Saxton 1993) that the relationship between the mean square displacement $\langle r^2 \rangle$ of a diffusing particle and the elapsed time t is given by Eq. (1):

$$\langle r^2 \rangle = 4Dt \tag{1}$$

where D represents the diffusion coefficient. Thus, we expect puncta whose motion is governed by simple diffusion to exhibit mean square displacements that are linear with respect to time. The relationship between mean square displacement and time for non-directional puncta (Fig. 2d) can be fitted to a linear function (Eq. (2); $r^2 = 0.970$).

$$\langle r^2 \rangle \left(\mu m^2\right) = (0.00213 \pm 0.00005)\,\mu m^2\ s^{-1} \times [\text{time(s)}] + (0.020 \pm 0.001)\,\mu m^2 \tag{2}$$

For directional puncta, the relationship can be fitted to a quadratic function (Eq. (3); $r^2 = 0.999$) or to a linear function (Eq. (4); $r^2 = 0.997$).

$$\langle r^2 \rangle \left(\mu m^2\right) = (-0.00056 \pm 0.00006)\,\mu m^2\ s^{-2} \times [\text{time (s)}]^2 + (0.139 \pm 0.002)\,\mu m^2\ s^{-1} \times [\text{time (s)}] - (0.02 \pm 0.02)\,\mu m^2 \tag{3}$$

$$\langle r^2 \rangle \left(\mu m^2\right) = (0.117 \pm 0.001)\,\mu m^2\ s^{-1} \times [\text{time (s)}] + (0.13 \pm 0.02)\,\mu m^2 \tag{4}$$

If both non-directional and directional puncta move under the influence of simple diffusion, then their diffusion coefficients should be identical, assuming that particles (e.g., vesicles) in both groups exhibit no difference in radius (Einstein 1905). Predicting diffusional movement in both groups, diffusion coefficients can be calculated from the slope of the best-fit line for the plot of mean square displacement of puncta against time using linear regression according to Eq. (1). The diffusion coefficient of directional puncta (2.92×10^{-10} cm s^{-1}) was found to be two orders of magnitude greater than that of non-directional puncta (5.4×10^{-12} cm s^{-1}), indicating that directional puncta mainly move via energy-dependent/active processes, while non-directional puncta primarily exhibit diffusional/passive movement.

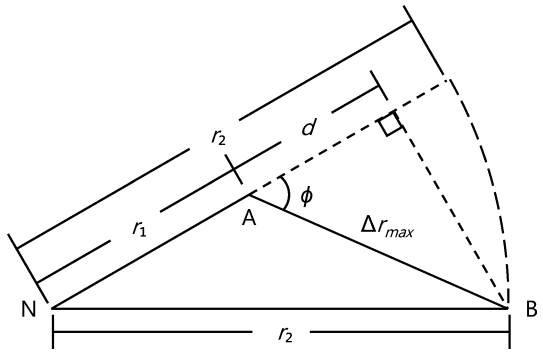

Fig. 3 Geometry of vesicular trafficking. The centroid of the nucleus is located at vertex N. The *vector* representing the maximal displacement Δr_{max} of a vesicle/punctum is defined by the endpoints A and B. r_1 represents the distance between the centroid of the nucleus and the earlier endpoint (point A) of the maximal displacement vector, and r_2 represents the distance between the centroid of the nucleus and the later endpoint (point B) of the maximal displacement vector. The *dashed curve* represents the rotation of the vector **NB** around an axis through N perpendicular to the page to assist in the visualization of the distances r_2 and r_1. The angle marked ϕ is the angle between the radial vector **NA** and the maximal displacement vector **AB** that defines the trajectory angle

A mean instantaneous speed was calculated for each punctum (Fig. 2e; see "Materials and methods"). The mean instantaneous speed of directional puncta (median 0.143 μm s^{-1}, IQR 0.103–0.213 μm s^{-1}) was significantly greater than that of non-directional puncta (median 0.052 μm s^{-1}, IQR 0.036–0.075 μm s^{-1}). This finding indicates that directional puncta exhibit greater mobility than non-directional puncta, as one would predict from the above-determined diffusion coefficients.

These results are in good agreement with previous studies of intracellular vesicular trafficking in cultured astrocytes, which studied pro-atrial natriuretic peptide (pro-ANP) fused to emerald green fluorescent protein (Emd; pro-ANP-Emd) (Potokar et al. 2005, 2007) and cannabinoid receptor 1 (CB1R) fused to EGFP (CB1R-EGFP) (Osborne et al. 2009). Thus, the movement of EAAT2-EGFP vesicles can be characterized as typical of intracellular trafficking of secretory vesicles.

Methods for the calculation of the trajectory angle

We used two different methods to measure the trajectory angles of the secretory vesicles using the geometry of vesicular trafficking: the first gives an accurate measurement of the trajectory angle (ϕ_E) and the second gives an approximation of the trajectory angle (ϕ_A), the details of which are discussed below.

Consider the scenario represented in Fig. 3 wherein vertex N represents the coordinates of the nucleus centroid, and vertices A and B represent the endpoints of the vector

corresponding to the maximal displacement of a punctum. The initial distance of the punctum from the nucleus centroid r_1 is the distance between points N and A, and the final distance of the punctum from the nucleus centroid $r_2$is the distance between points N and B. The angle ϕ between the radial vector **NA** and the maximal displacement vector **AB** is given by

$$\phi = \arccos\left(\frac{d}{\Delta r_{\max}}\right) \tag{5}$$

Using the law of cosines, this expression can be rewritten in terms of r_1 and r_2 that are directly measureable for trafficking puncta to obtain the accurate trajectory angle, ϕ_{E}:

$$\phi_{\mathrm{E}} = \arccos\left(\left|\frac{r_2^2 - r_1^2 - \Delta r_{\max}^2}{2 r_1 \Delta r_{\max}}\right|\right) \tag{6}$$

Equation (6) accurately defines the magnitude of the trajectory angle. However, this expression is computationally complex.

If the distance between the punctum and the nucleus centroid is much greater than the maximal displacement (i.e., $r_1 \gg \Delta r_{\max}$), then $d \approx r_2 - r_1$. In such a case, the expression for the magnitude of the trajectory angle (ϕ_{A}) can be approximated to

$$\phi_{\mathrm{A}} = \arccos\left(\left|\frac{r_2 - r_1}{\Delta r_{\max}}\right|\right) \tag{7}$$

Equations (6) and (7) provide two different expressions for the calculation of the magnitude of the trajectory angle. Equation (7) is computationally less complex and hence more efficient, i.e., less time consuming; however, it is based on an approximation and thus includes some error. We investigated this error further in the next section.

We assigned positive angles to puncta moving away from the nucleus and negative angles to the puncta moving toward the nucleus. Thus, puncta which move directly away from or toward the centroid of the nucleus have trajectory angles of ±0°, and puncta which move in a tangential direction with respect to the centroid of the nucleus have trajectory angles of ±90°. If the x coordinate of one endpoint of the maximal displacement vector was exactly equal to that of the other endpoint, the custom script used to calculate the trajectory angle threw an error and the punctum (4 of 2593 studied; relevant to trajectory angles below, one punctum was directional) was excluded from angle analysis.

Distribution of trajectory angles for directional vesicles

As it is assumed that directional vesicles, undergoing active movement, are those that interact with cytoskeletal elements, we determined the distribution of trajectory angles for directional puncta. Trajectory angles for directional puncta in all the cells were calculated using both the exact (Eq. (6)) and approximate (Eq. (7)) methods and grouped into bins of 10° (Fig. 4). One directional punctum out of 1,110 was excluded from angle analysis because the custom script used could

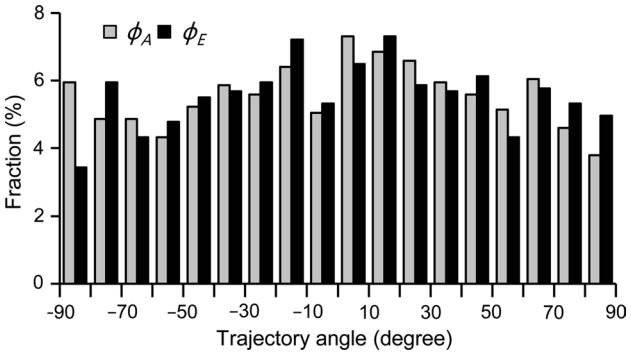

Fig. 4 Distribution of trajectory angles. Frequency of trajectory angles calculated using the exact (ϕ_{E}) and approximate (ϕ_{A}) methods for directional puncta as a percentage of all puncta for which trajectory angles could be calculated (n = 1,109 for 15 cells). *Solid black bars* represent ϕ_{E}, and *solid gray bars* represent ϕ_{A}. Both distributions were found to be non-normal ($p < 0.01$) and unimodal ($p > 0.05$) (color figure online)

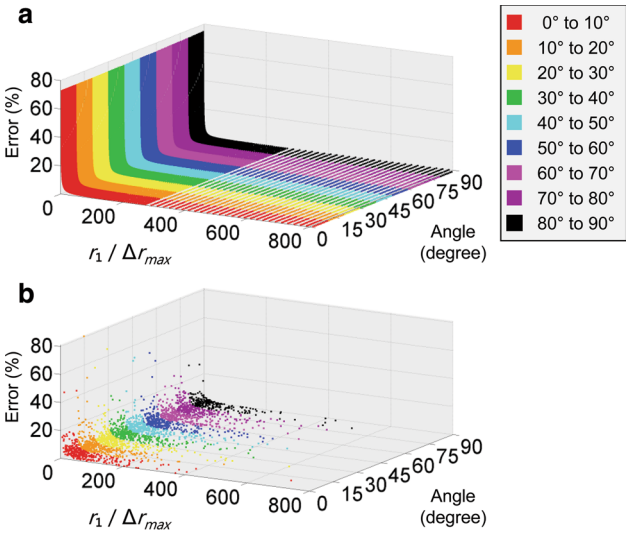

Fig. 5 Dependence of the error between the approximate and exact methods of calculating the trajectory angle on trafficking parameters. **a** Plot of the simulation of the error between the trajectory angles calculated using the exact and approximate methods as a function of the magnitude of the trajectory angle ϕ_{E} and of the ratio of the initial distance of the punctum from the nucleus to the maximal displacement of the punctum, $r_1/\Delta r_{\max}$. Apparent striations result from the sampling of lesser data points in the range of higher $r_1/\Delta r_{\max}$ ratios, consistent with experimental data. **b** Plot of the experimental data of the error between the trajectory angles calculated using the exact and approximate methods as a function of ϕ_E and $r_1/\Delta r_{\max}$ (n = 2,587 for 15 cells). *Colors* in **a** and **b** correspond to the magnitude of the trajectory angle (see *inset*)

not calculate the trajectory angle (see above). The resulting distributions for the two methods were determined to be non-normal but unimodal. Rounding each angle to the nearest 1°, the mode of the distribution for ϕ_E was 19°, and the mode of the distribution for ϕ_A was 9°. The discrepancy between the distributions seems to be larger at angles closer to ±90°, suggesting that the error between the approximate and exact methods may have an angular dependence.

Dependence of the error between the exact and approximate methods of calculating the trajectory angle on trafficking parameters

We next examined the parameters that influence the magnitude of the error between the approximate and the exact methods of calculating the trajectory angle. The approximation used in the calculation of the trajectory angle by the approximate method relies on the ratio of the initial distance of the punctum from the nucleus centroid to the maximal displacement of the punctum ($r_1/\Delta r_{max}$). Thus, we hypothesized that the error is a function of this ratio and of the magnitude of the trajectory angle. A simulation was performed by varying r_1 between 1 and 81 μm, Δr_{max} between 0.1 and 12.1 μm, and ϕ_E between 0.5° and 89.5° (these ranges correspond to the ranges of values found in the set of 15 cells used for the analysis) and then calculating the percentage error for each combination of the values. The resulting plot, shown in Fig. 5a, demonstrated that the simulated error exhibited an inverse dependence on the ratio $r_1/\Delta r_{max}$ and did not exhibit a substantial dependence on the magnitude of the trajectory angle.

The same quantities were plotted using the experimental data (Fig. 5b). As before, four puncta were excluded because the custom script used could not calculate the trajectory angle, and two additional puncta were disqualified as outliers (errors 1,768.5 and 819.8 %; errors for the other puncta were less than 80.6 %) so that further error analysis was performed on 2,587 puncta. The experimental error exhibited an inverse dependence on the ratio $r_1/\Delta r_{max}$ and a lack of substantial dependence on the magnitude of the trajectory angle, a finding in agreement with the simulation data. Thus, we concluded that the ratio $r_1/\Delta r_{max}$ has a much greater influence on the error between the two methods of calculating the trajectory angle than the magnitude of the trajectory angle. Consequently, the discrepancies in the distributions in Fig. 4 can likely be attributed to the differences in $r_1/\Delta r_{max}$ at different angles.

Quantification of the error between the exact and approximate methods of calculating the trajectory angle: determination of exclusion distance

To further investigate the dependence of the error between the two methods on the ratio $r_1/\Delta r_{max}$, we plotted the

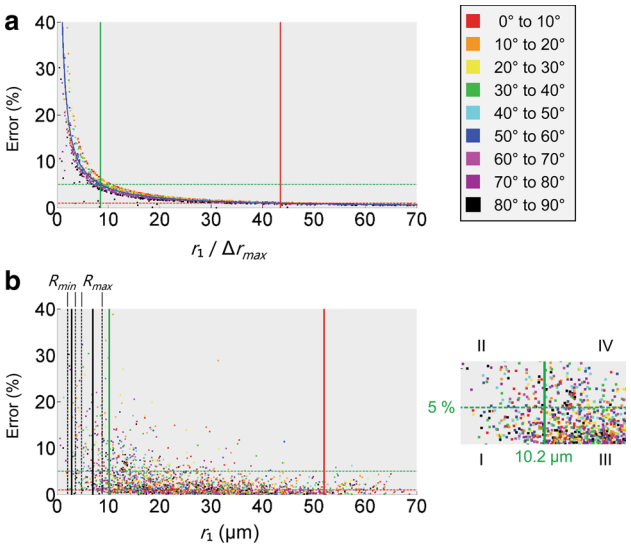

Fig. 6 Exclusion distance. **a** Plot of the error between the approximate and exact methods as a function of the ratio of the initial distance of the punctum from the nucleus to the maximal displacement of the punctum $r_1/\Delta r_{max}$. The *blue curve* represents the function given in Eq. (8). The *horizontal dashed lines* represent threshold error values of 5 % (*green*) and 1 % (*red*), and the *vertical solid lines* represent the values of $r_1/\Delta r_{max}$ that correspond to those error values. **b** Plot of the error as a function of the initial distance of the punctum from the nucleus centroid r_1. The *vertical solid black* lines represent the median values of the maximum nuclear radius R_{max} (7.0 μm) and the minimum nuclear radius R_{min} (2.9 μm), and the *vertical dashed black lines* represent the interquartile ranges (4.8–8.8 μm for R_{max} and 2.1 and 3.6 μm for R_{min}). The *horizontal dashed lines* represent threshold error values of 5 % (*green*) and 1 % (*red*), and the *vertical solid lines* represent the values of r_1 that correspond to those error values. *Inset* represents a close-up of the *green lines* crosshair, which in turn demarcates four classes of puncta (I–IV; see text for details) based on their error compared to the 5 % threshold and their position compared to the corresponding value of r_1 (color figure online)

percentage error as a function of $r_1/\Delta r_{max}$ only (Fig. 6a). This data was fitted ($r^2 = 0.964$) to a power function given by Eq. (8):

$$\text{Error (\%)} = (41.46 \pm 0.01)\left(\frac{r_1}{\Delta r_{max}}\right)^{-0.987 \pm 0.004} \quad (8)$$

This fitting function was used to determine the value of $r_1/\Delta r_{max}$ that produces an acceptable error, i.e., 1 or 5 %. For error threshold values of 5 and 1 %, the corresponding values of $r_1/\Delta r_{max}$ were 8.53 and 43.5, respectively.

To express these values in terms of the distance from the nucleus centroid, we multiplied them by the mean maximal displacement, 1.20 μm. The resulting values of r_1 were 10.2 μm for a 5 % acceptable error and 52 μm for a 1 % acceptable error (Fig. 6b, vertical green and red lines, respectively, corresponding to error level indicated by matching horizontal lines); as one would expect, both

values exceed the nucleus boundary based on the measured radii of the nuclei (Fig. 6b, black vertical lines; for details see figure legend). These values represent the exclusion distances for a given acceptable error; the exclusion distance is the minimum distance from the nucleus centroid at which the approximate method of calculating the trajectory angle can be used with reasonable confidence that the error will be less than the acceptable error for that exclusion distance.

The validity of the exclusion distance was verified by comparing the number of puncta with errors above the acceptable error value to the number of puncta with errors below the acceptable error value. The puncta were classified into four groups based on delineating them by the 5 % error and its exclusion distance (shown in Fig. 6b inset as a green crosshair): (a) group I contains puncta located closer to the nucleus centroid than the exclusion distance whose error is less than 5 %; (b) group II contains puncta located closer to the nucleus centroid than the exclusion distance whose error is greater than 5 %; (c) group III contains puncta located farther from the nucleus centroid than the exclusion distance whose error is less than 5 %; and (d) group IV contains puncta located farther from the nucleus centroid than the exclusion distance whose error is greater than 5 % (Fig. 6b, inset). The number of puncta is 133 (5.1 % of all puncta selected for error analysis) in group I, 145 (5.6 %) in group II, 2,062 (79.7 %) in group III, and 247 (9.5 %) in group IV. For puncta closer to the nucleus centroid than the exclusion distance (groups I and II), the fraction of puncta with an error greater than 5 % (group II) is 0.522; for puncta farther from the nucleus centroid than the exclusion distance (group III and IV), the fraction of puncta with an error greater than 5 % (group IV) is 0.107, however. Thus, using the approximate method is much more likely (52.2 vs 10.7 %) to produce an error in the calculated trajectory angle greater than the 5 % error threshold when the punctum is closer to the nucleus centroid than the exclusion distance. The exclusion distance, then, is a good parameter for predicting the accuracy of the approximate method.

Discussion

We monitored the trafficking of intracellular vesicles containing EAAT2-EGFP and implemented two methods for calculating their trajectory angles. We determined that these vesicles exhibit similar trafficking behavior as other intracellular vesicles in astrocytes in that the population of vesicles can be classified into non-directional vesicles whose movement is diffusional and directional motion whose movement is directed, likely by active transport along cytoskeletal tracts. Directional vesicles exhibit greater directionality indices and mean instantaneous speeds than non-directional vesicles.

We recommend an exclusion distance from the nucleus centroid to determine which of the two methods should be used to calculate the trajectory angle of trafficking vesicles. The exact method given in Eq. (6) should be used for vesicles closer to the nucleus centroid than the exclusion distance (albeit this method can be used for vesicles at farther/any distance from the nucleus), and the approximate method given in Eq. (7) should be used for vesicles farther from the nucleus centroid than the exclusion distance. This choice of methodology will reduce the computation time required to analyze large amounts of trafficking data while simultaneously reducing the error in the analysis. In this study, 10.7 % of puncta begin their trajectory closer than the exclusion distance for 5 % error. Thus, if all puncta had been analyzed using the approximate method, a significant portion of the data would have produced errors above the acceptable error value. The 5 % error threshold was chosen over the 1 % error threshold because 95 % of vesicles in our study were closer to the nucleus centroid than the exclusion distance for an acceptable error of 1 %, making this distance impractical for minimizing computation time. Consequently, the 5 % error threshold and the corresponding exclusion distance provide the best balance of minimizing computational error and minimizing error. Experimentalists who wish to further reduce computational time at the expense of accuracy or to further reduce error at the expense of computational time can adjust the exclusion distance according to their needs by choosing a different threshold of acceptable error and repeating the procedure carried out in the previous section.

Since the analysis for vesicular trafficking was done in 2D rather than 3D, there is a possibility of an additional axial error in our measurements; however, the thin areas (approximately 1 μm) of cultured astrocytes used for analysis greatly limit the motion of vesicles in the direction perpendicular to the imaging plane. Thus, this motion is unlikely to significantly affect the measurement of punctum mobility (Potokar et al. 2005).

The ability of effectively calculating the trajectory angles of secretory vesicles is useful in studying vesicular trafficking because it provides an insight into the types of cytoskeletal elements used for the trafficking of that vesicle (Osborne et al. 2009). It is known that microtubules are arranged radially, i.e., at 0°, with respect to the microtubule organizing center near the nucleus (Darnell et al. 1990). It is likely that directional vesicles whose trajectory angles closely match 0° are being actively transported along microtubules.

Although well characterized in other cells, the mechanisms underlying secretory vesicle trafficking are not clear in astrocytes. Microtubules and actin filaments are involved

in vesicle trafficking in most types of cells (Caviston and Holzbaur 2006; Krendel and Mooseker 2005), but there has been evidence that secretory vesicles in astrocytes also rely on the intermediate filaments glial fibrillary acidic protein (GFAP) and vimentin (Kreft et al. 2009; Potokar et al. 2007), the former being a cell-specific marker for astrocytes. Characterization of the mechanisms utilized for intracellular trafficking has important physiological implications because the pathology of several diseases of the nervous system has been linked to cytoskeleton dysfunction. Most notably, Alexander disease, characterized by the presence of Rosenthal fibers in astrocytes, has been linked to both mutations in GFAP (Brenner et al. 2001) and to glutamate-induced excitotoxicity (Tian et al. 2010). Understanding the physiological mechanisms of vesicle trafficking and their relationship with the astrocytic cytoskeleton may elucidate interventions that can be made to treat diseases such as Alexander disease.

A subject in need of further study is the nature of the distribution of trajectory angles with respect to the trans-Golgi network (TGN). All secretory vesicles are packaged by the TGN before they are released to diffuse freely in the cytoplasm or to be transported along the cytoskeleton. Although the microtubules are arranged around the microtubule organizing center anchored near the nucleus, we speculate that other cytoskeletal filaments may be arranged around the TGN instead. If the TGN can be found to be an epicenter of trafficking for a subset of vesicles, then it is likely that those vesicles utilize filaments other than microtubules for their trafficking.

Although this study examined EAAT2-EGFP vesicles trafficked in cultured astrocytes, the methodology described in this paper is relevant to other trafficking vesicles and other types of cells. The mechanisms underlying secretory vesicle trafficking are nearly universal in mammalian cells, so the recommendations given here are applicable to any cell that utilizes the secretory/exocytotic pathway; the majority of ~200 cell types present in the human body utilize this pathway.

Acknowledgments We thank Dr. Jeffrey D. Rothstein for providing the EAAT2-EGFP plasmid. We also thank Erik Malarkey for his assistance with the initial vesicle trafficking protocols. This study was funded by the National Institutes of Health (The Eunice Kennedy Shriver National Institute of Child Health and Human Development award HD078678).

Conflict of interest The authors declare that they have no conflict of interest.

Ethical standard All applicable international, national, and/or institutional guidelines for the care and use of animals were followed. All procedures performed in studies involving animals were in accordance with the ethical standards of the institution or practice at which the studies were conducted.

References

Brenner M, Johnson AB, Boespflug-Tanguy O, Rodriguez D, Goldman JE, Messing A (2001) Mutations in GFAP, encoding glial fibrillary acidic protein, are associated with Alexander disease. Nat Genet 27:117–120. doi:10.1038/83679

Cavender CE, Gottipati MK, Malarkey EB, Parpura V (2013) Method for the determination of trajectory angles of directional secretory vesicles in cultured astrocytes. Inquiro 7:48–52

Caviston JP, Holzbaur EL (2006) Microtubule motors at the intersection of trafficking and transport. Trends Cell Biol 16:530–537. doi:10.1016/j.tcb.2006.08.002

Danbolt NC (2001) Glutamate uptake. Prog Neurobiol 65:1–105

Darnell J, Lodish H, Baltimore D (1990) Molecular cell biology, 2nd edn. Scientific American Books Inc., New York

Drummond GB (2009) Reporting ethical matters in the Journal of Physiology: standards and advice. J Physiol 587:713–719

Einstein A (1905) On the movement of small particles suspended in stationary liquids required by the molecular-kinetic theory of heat. Ann Phys 17:549–560

Furuta A, Rothstein JD, Martin LJ (1997) Glutamate transporter protein subtypes are expressed differentially during rat CNS development. J Neurosci 17:8363–8375

Gottipati MK, Kalinina I, Bekyarova E, Haddon RC, Parpura V (2012) Chemically functionalized water-soluble single-walled carbon nanotubes modulate morpho-functional characteristics of astrocytes. Nano Lett 12:4742–4747. doi:10.1021/nl302178s

Hartigan JA, Hartigan PM (1985) The dip test of unimodality. Ann Stat 13:70–84. doi:10.2307/2241144

Haydon PG, Lartius R, Parpura V, Marchese-Ragona SP (1996) Membrane deformation of living glial cells using atomic force microscopy. J Microsc 182:114–120

Hertz L, Dringen R, Schousboe A, Robinson SR (1999) Astrocytes: glutamate producers for neurons. J Neurosci Res 57:417–428

Hughes EG, Maguire JL, McMinn MT, Scholz RE, Sutherland ML (2004) Loss of glial fibrillary acidic protein results in decreased glutamate transport and inhibition of PKA-induced EAAT2 cell surface trafficking. Brain Res Mol Brain Res 124:114–123. doi:10.1016/j.molbrainres.2004.02.021

Hynd MR, Scott HL, Dodd PR (2004) Glutamate-mediated excitotoxicity and neurodegeneration in Alzheimer's disease. Neurochem Int 45:583–595. doi:10.1016/j.neuint.2004.03.007

Kreft M, Potokar M, Stenovec M, Pangrsic T, Zorec R (2009) Regulated exocytosis and vesicle trafficking in astrocytes. Ann N Y Acad Sci 1152:30–42. doi:10.1111/j.1749-6632.2008.04005.x

Krendel M, Mooseker MS (2005) Myosins: tails (and heads) of functional diversity. Physiology 20:239–251. doi:10.1152/physiol.00014.2005

Lau A, Tymianski M (2010) Glutamate receptors, neurotoxicity and neurodegeneration. Pflugers Arch 460:525–542. doi:10.1007/s00424-010-0809-1

Lee W, Parpura V (2012) Dissociated cell culture for testing effects of carbon nanotubes on neuronal growth. Methods Mol Biol 846:261–276

Malarkey EB, Parpura V (2011) Temporal characteristics of vesicular fusion in astrocytes: examination of synaptobrevin 2-laden vesicles at single vesicle resolution. Journal Physiol 589:4271–4300. doi:10.1113/jphysiol.2011.210435

McCarthy KD, de Vellis J (1980) Preparation of separate astroglial and oligodendroglial cell cultures from rat cerebral tissue. J Cell Biol 85:890–902

Montana V, Ni Y, Sunjara V, Hua X, Parpura V (2004) Vesicular glutamate transporter-dependent glutamate release from astrocytes. J Neurosci 24:2633–2642. doi:10.1523/JNEUROSCI.3770-03.2004

Nedergaard M, Ransom B, Goldman SA (2003) New roles for astrocytes: redefining the functional architecture of the brain. Trends Neurosci 26:523–530. doi:10.1016/j.tins.2003.08.008

Osborne KD, Lee W, Malarkey EB, Irving AJ, Parpura V (2009) Dynamic imaging of cannabinoid receptor 1 vesicular trafficking in cultured astrocytes. ASN Neuro. doi:10.1042/AN20090040

Parpura V, Verkhratsky A (2012) Homeostatic function of astrocytes: Ca(2+) and Na(+) signalling. Translational neuroscience 3:334–344. doi:10.2478/s13380-012-0040-y

Potokar M, Kreft M, Pangrsic T, Zorec R (2005) Vesicle mobility studied in cultured astrocytes. Biochem Biophysical Res Commun 329:678–683. doi:10.1016/j.bbrc.2005.02.030

Potokar M et al (2007) Cytoskeleton and vesicle mobility in astrocytes. Traffic 8:12–20. doi:10.1111/j.1600-0854.2006.00509.x

Reyes RC, Perry G, Lesort M, Parpura V (2011) Immunophilin deficiency augments Ca2+ -dependent glutamate release from mouse cortical astrocytes. Cell Calcium 49:23–34

Rothstein JD et al (1996) Knockout of glutamate transporters reveals a major role for astroglial transport in excitotoxicity and clearance of glutamate. Neuron 16:675–686

Saxton MJ (1993) Lateral diffusion in an archipelago. Single-particle diffusion. Biophys J 64:1766–1780. doi:10.1016/S0006-3495(93)81548-0

Singh P et al (2014) Single-vesicle architecture of synaptobrevin 2 in astrocytes. Nature Commun 5:3780. doi:10.1038/ncomms4780

Tian R, Wu X, Hagemann TL, Sosunov AA, Messing A, McKhann GM, Goldman JE (2010) Alexander disease mutant glial fibrillary acidic protein compromises glutamate transport in astrocytes. J Neuropathol Exp Neurol 69:335–345. doi:10.1097/NEN.0b013e3181d3cb52